SCIENCE CHINA
Information Sciences

• RESEARCH PAPER •

January 2021, Vol. 64 112209:1–112209:14
https://doi.org/10.1007/s11432-019-2824-y

Angular velocity estimation using characteristics of star trails obtained by star sensor for spacecraft

Xiaolin NING[1*], Pingping CHEN[1], Yueqing HUANG[1*], Weiren WU[2] & Jiancheng FANG[1]

[1]*School of Instrumentation Science & Opto-electronics Engineering, Beihang University, Beijing* 100191*, China;*
[2]*Lunar Exploration and Space Program Center, China National Space Administration, Beijing* 100037*, China*

Received 10 October 2019/Revised 25 January 2020/Accepted 29 February 2020/Published online 24 December 2020

Abstract Many studies have been conducted about angular velocity estimation using star sensors, and fairly good performance is achieved when the spacecraft is working at low-dynamic environments. However, when the spacecraft rotates at a large angular velocity, the star image will become blurred, which makes it difficult to identify and recognize star centroids, which, in turn, reduces the accuracy of angular velocity estimation. Therefore, to solve the problem with angular velocity estimation in highly dynamic situations, this research studies a method of angular velocity estimation using blurred star images. The length and ending point coordinates of star trails obtained from these blurred star images are used for a series of processes, which includes the pre-processing of blurred star images, determination of starting and ending points, thinning and selection of star trails, and calculation of trail lengths. Simulations show that the effectiveness of the proposed method in highly dynamic situations and the angular velocity estimation errors in constant and sinusoidal variation are reduced by at least 66% and 62%, respectively, compared with those of the traditional method.

Keywords angular velocity estimation, star sensor, blurred star images, star trail characteristics, unscented Kalman filter

Citation Ning X L, Chen P P, Huang Y Q, et al. Angular velocity estimation using characteristics of star trails obtained by star sensor for spacecraft. Sci China Inf Sci, 2021, 64(1): 112209, https://doi.org/10.1007/s11432-019-2824-y

1 Introduction

Angular velocity is one of the most important attitude parameters, which generally can be output by the gyroscope equipped on a spacecraft [1]. However, gyroscopes are inevitably affected by problems with high cost, drift, and noise [2]. Therefore, to solve these problems, gyro-less angular velocity estimation methods have gradually been developed to become more effective and have been used as substitutes when gyroscopes are not sufficiently functional [3]. For example, the angular velocity and acceleration can be obtained from accelerometer outputs [4]. The attitude and angular velocity of low-earth orbiting (LEO) spacecraft can be determined by a three-axis magnetometer [5]. Meanwhile, the angular velocity can be derived by star sensors [6] using the derivative method [7,8] and estimation method [9,10].

In the derivative method, angular velocity can be obtained via differentiation of the attitude angle and through the use of kinematic equations when the attitude of the spacecraft is known [10]. Because star sensors often have the best accuracy in attitude estimation [11], they are widely used in spacecraft attitude estimation systems. For example, the latest widely used Astro 15 is determined to have an attitude accuracy of the xy-axes that is less than 1 arcsec 1δ and of the z-axis that is less than 10 arcsec 1δ, with a sampling time of 0.25 s [12].

On the other hand, the spacecraft attitude determination method based on star sensors obtains the vector information of the observed star through star sensor measurements; after the image centroiding [12–14] and star identification processes [15,16], the navigation star vector information of the corresponding

* Corresponding author (email: ningxiaolin@buaa.edu.cn, sy1917224@buaa.edu.cn)

celestial coordinate system is identified. Through the use of the corresponding attitude determination algorithm [16–18], the attitude of the spacecraft in the relative celestial coordinate system is determined. In the estimation method, attitude determination and star recognition are not necessary; the star vector [9] and optical flow [19, 20] are widely used measurements. In addition, Roshannian et al. [21] proposed for the measurement process the use of the displacement of the center of window, which is calculated via the particle image velocimetry (PIV) technique, in two continuous clear star images.

However, when the spacecraft rotates with a large angular velocity, the star point will be a streak across the star image, which will then produce a blurred star image. The blurred star image results in the loss of precision of the centroid of the star, which causes reduced accuracy of attitude determination and angular velocity estimation. Moreover, blurred star images will usually require image restoration [22,23], a process that is cumbersome and requires more calculations to determine attitude information and angular velocity information [24].

There are several methods for estimating attitude angular velocity directly using blurred star images. For example, Accardo [25] computed the velocity vector using the coordinates of the start and end points of star trails from blurred star images acquired during fast rotations (2°–8° per second), and estimated the angular velocity using this velocity vector and the least square method. In this method, each star trail is regarded as a line, which simplifies the calculation but cannot accurately describe the real trail of the star when the trail is non-line or arc-shaped. On the other hand, Fasano et al. [26] proposed a spacecraft angular velocity estimation method using blurred star images, that uses the optical flow field calculated using sequences of the blurred star images to evaluate the velocity vector, and then uses this velocity vector to estimate angular velocity. However, a matching error exists in the region-based optical flow calculation, and the estimation performance decreases with the increase in angular velocity. Fasano's method and Accardo's method are similar to each other, except for the way of obtaining the velocity vector.

As mentioned previously, angular velocity estimation under highly dynamic conditions is an urgent problem that needs to be solved. Therefore, for spacecraft, a new angular estimation method using the characteristics of star trails directly obtained from blurred star images is proposed in this paper. These characteristics, including the length and the coordinates of the ending point of the star trail, are used and can be obtained through the pre-processing of star images, determination of starting and ending points, thinning and selection of star trails, and calculations of trail lengths. The Singer acceleration probability model is used as the state model. The relationship between the measurement and the angular velocity of spacecraft is established and then used to predict the measurement according to the state instead of using the traditional measurement model. The unscented Kalman filter is used to estimate the angular velocities and angular accelerations of the three axes of the spacecraft. Simulations demonstrate that the proposed method exhibits high accuracy of angular velocity estimation in highly dynamical conditions. The estimation errors are reduced by at least 66% compared to those of Accardo's method.

This paper is systematized into five sections. After this introduction, the method of measurement of trail characteristics is given in Section 2. The angular velocity estimation for spacecraft using the characteristics of star trails is introduced in detail in Section 3. Simulations and analysis are shown to demonstrate the feasibility of the proposed method in Section 4. At the end, a conclusion is drawn in Section 5.

2 Determination of characteristics of star trails

The measurement acquisition process for the star trail characteristics, as summarized in Figure 1, includes the pre-processing of blurred star images, determination of starting and ending points, thinning and selection of star trails, and calculation of trail lengths. The length and coordinates of the ending point of the star trail are acquired from blurred star images and are used in the estimation.

2.1 Pre-processing of blurred star images

The obtained original blurred star image at time t_k is expressed as $z_k(u, v)$, and the origin is in the top left corner (u, v), represented in pixel coordinates.

The obtained blurred star image usually consists of star trails and noises. The background signal and noises, whose brightness is weaker than the stars, should be removed. The Otsu threshold segmentation is used to reduce the background signal and noises [27]:

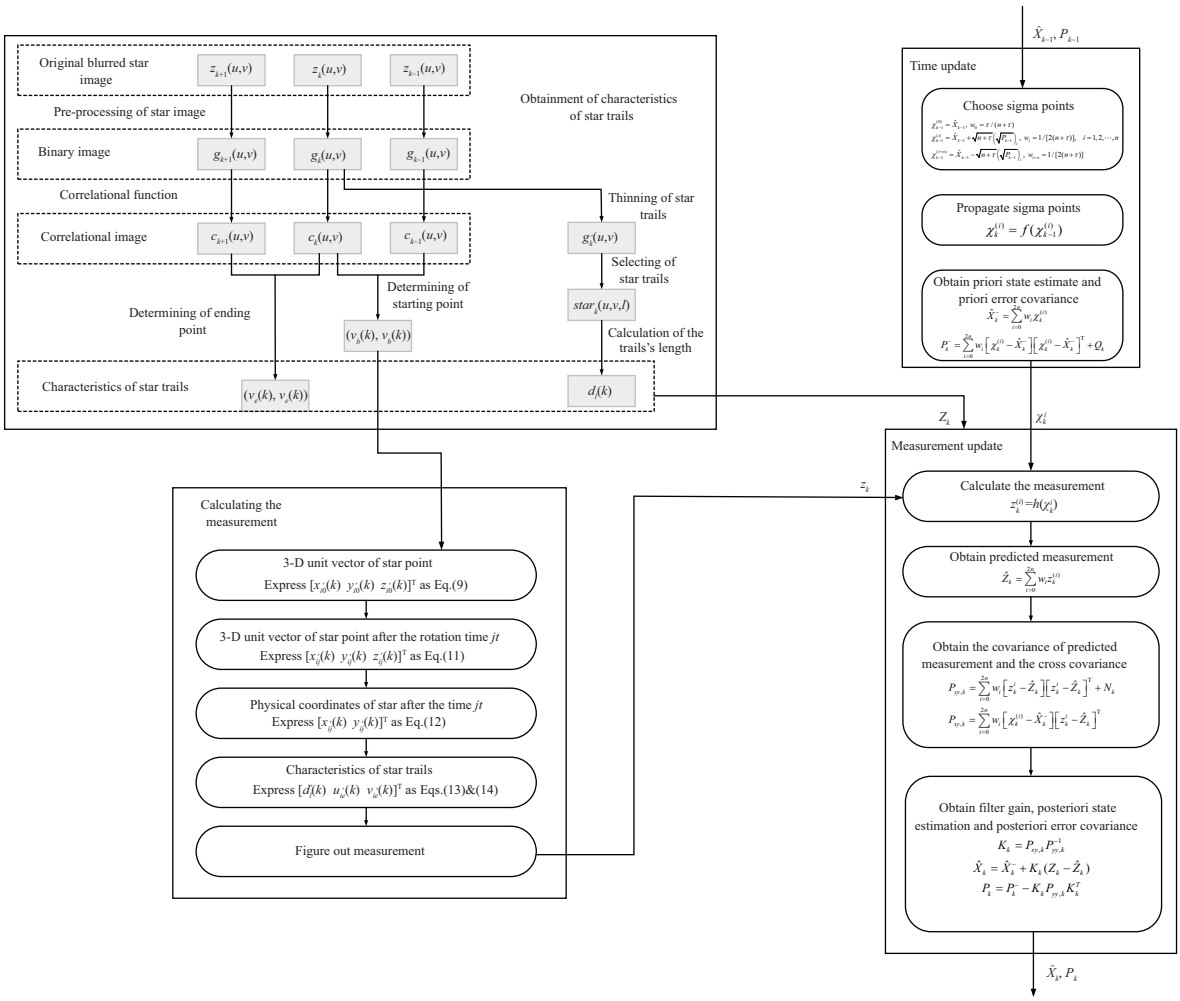

Figure 1 Flowchart of the process of obtaining the characteristics of star trails, and diagram of the filter schematic.

$$z'_k(u,v)=\begin{cases} z_k(u,v)-T_{\text{back}}, & T_{\text{back}}\leqslant z_k(u,v),\\ 0, & T_{\text{back}}>z_k(u,v), \end{cases} \tag{1}$$

where $z'_k(u,v)$ is the star image after segmentation, and T_{back} is the threshold.

For the determination of the value of T_{back}, a method based on maximum inter-class variance is used here, with the details of the method as follows [28]:

(1) The pixels of a given picture are represented by gray levels, and the gray-level histogram is normalized using a probability distribution.

(2) Based on a threshold k, pixels are dichotomized into two classes: background and object.

(3) This method can determine the probabilities of class occurrence and the class mean levels, the zeroth and the first-order cumulative moments of the histogram up to the k-th level, the total mean level of the original picture, and the class variances.

(4) This method also introduces discriminant criterion measures (or measures of class separability).

(5) This method can get the within-class variance, between-class variance, and total variance of levels.

Our problem is then reduced to an optimization problem to search for a threshold k that maximizes one of the object functions (the criterion measures).

Binarization processing is then performed to convert grayscale image $z'_k(u,v)$ into binary image $g_k(u,v)$, to simplify calculations, highlight the star trails, and facilitate subsequent image processing.

2.2 Determination of starting and ending points

To avoid the inability of finding the starting and ending points caused by an image lag of sensors [29], a correlational function is used to enhance the star trail boundary, which is expressed as follows [30]:

$$\begin{aligned} c_k(u,v) &= h(m,n) \times g_k(u,v), \\ &= \sum_{m=-a}^{a} \sum_{n=-b}^{b} h(m,n) g_k(u+m, v+n), \end{aligned} \tag{2}$$

where the filter template $h(m,n)$ adopts an $A \times B$ window and is basically consistent with star point energy distribution, assuming that A and B are odd integers, $a = \frac{A-1}{2}$, $b = \frac{B-1}{2}$, and $c_k(u,v)$ is the correlational image.

Because the boundary of the star point areas is filled with pixels after correlation filter processing, the white points at the same coordinates in consecutive star images $c_{k-1}(u,v)$ and $c_k(u,v)$ are found, and the starting points are selected from $(u_b(k), v_b(k)) = c_{k-1}(u,v) \bigcap c_k(u,v)$ [30]. The ending points can also be selected from $(u_e(k), v_e(k)) = c_k(u,v) \bigcap c_{k+1}(u,v)$ in the same way. Generally, the ending point of the trail of the same star in $c_k(u,v)$ is the starting point of the trail in the $c_{k+1}(u,v)$ image, and thus the ending points of the k-th time instant can be exploited as starting points of the $(k+1)$-th time instant. Because some of the starting and ending positions selected have multiple discrete coordinates, the moment center method is used to extract the centroid [27].

2.3 Thinning and selection of star trails

Because of the influence of the point spread function (PSF) on the star points, a thinning algorithm is necessary before the star trail labeling process [31]. The star image after the thinning process is recorded as $g'_k(u,v)$. The 8-connected region labeling algorithm is then used to label the star trails of $g'_k(u,v)$ [30]. All the pixel coordinates of each star trail will then be saved after the trail labeling.

Because of the rotation of the spacecraft, stars may be move out of or come into the field of view (FOV) during exposure time, and different trails may end up overlapping. Only the star trails that are within the FOV during exposure time and are not overlapped during the whole exposure period are preserved.

Finally, the star trails meeting the requirement are selected and labeled. A series of pixel coordinates from each trail can be obtained and saved in a 3D array expressed as $\mathrm{star}_k(u,v,l)$, where l $(l = 1, 2, \ldots, p)$ represents the number of star trails.

2.4 Calculation of trail lengths

The length of the star trail l can be calculated using the star coordinates of each trail obtained using the previously described method. To simplify the calculation, each trail is divided into 10 segments according to the coordinates. If there is a larger variation in the horizontal coordinates, 10 uniformly distributed u coordinates can be obtained as $u_{l_j}(k) = \frac{u_{l_b}(k) + j(u_{l_e}(k) - u_{l_b}(k))}{10}, j = 1, \ldots, 10$. The corresponding $v_{l_j}(k)$ on the trail can then be found, with the Euclidean distance between two adjacent coordinates as the approximate length of each segment, and thus the trail length $d_l(k)$ can be calculated as follows:

$$\begin{aligned} d_l(k) =& \sqrt{(u_{l_1}(k) - u_{l_b}(k))^2 dx^2 + (v_{l_1}(k) - v_{l_b}(k))^2 dy^2} \\ &+ \sqrt{(u_{l_2}(k) - u_{l_1}(k))^2 dx^2 + (v_{l_2}(k) - v_{l_1}(k))^2 dy^2} + \cdots \\ &+ \sqrt{(u_{l_e}(k) - u_{l_9}(k))^2 dx^2 + (v_{l_e}(k) - v_{l_9}(k))^2 dy^2}, \end{aligned} \tag{3}$$

where dy, dx represent the physical size of each pixel element. Similarly, if the variation in vertical difference is larger, 10 uniformly distributed v coordinates can be obtained.

In addition, because the length calculation accuracy will decrease when the star trail is short, a judgment process is necessary. If $d_l(k)$ is less than a threshold d_T, which is set to 20 pixels, the trail will be deleted.

2.5 Obtaining the measurement

With the use of the length and coordinates of the ending points of the l-th star trail, the measurement in the k-th time instant is regarded as

$$\boldsymbol{Z}_l(k) = \begin{bmatrix} d_l(k) \\ u_{l_e}(k) \\ v_{l_e}(k) \end{bmatrix}. \tag{4}$$

All the measurements in the k-th time instant can be expressed as

$$\boldsymbol{Z}(k) = \begin{bmatrix} \boldsymbol{Z}_1(k) \\ \boldsymbol{Z}_2(k) \\ \vdots \\ \boldsymbol{Z}_p(k) \end{bmatrix}. \tag{5}$$

3 Angular velocity estimation using characteristics of star trails for spacecraft

3.1 State model

The Singer acceleration probabilistic model is chosen to be the state model in this study [32]:

$$\boldsymbol{X}_k = \boldsymbol{\Phi}_T \boldsymbol{X}_{k-1} + \boldsymbol{W}_{k-1}, \tag{6}$$

$$\boldsymbol{\Phi}_T = \begin{bmatrix} \boldsymbol{I} & \boldsymbol{\Lambda}^{-1}(\boldsymbol{I} - \mathrm{e}^{-\boldsymbol{\Lambda} T}) \\ 0 & \mathrm{e}^{-\boldsymbol{\Lambda} T} \end{bmatrix}, \tag{7}$$

where $\boldsymbol{X}_k = [w_x(k), w_y(k), w_z(k), w'_x(k), w'_y(k), w'_z(k)]^{\mathrm{T}}$ is the state vector, $w_x(k)$, $w_y(k)$, and $w_z(k)$ are the angular velocities around the three axes in body frame, and $w'_x(k)$, $w'_y(k)$, and $w'_z(k)$ are the angular accelerations. $\boldsymbol{\Phi}_T$ is the state transition matrix, $\boldsymbol{W}_{k-1}$ is the process noise, and $\boldsymbol{I}$ is a 3×3 identity matrix. $\boldsymbol{\Lambda} = \mathrm{diag}(\frac{1}{\tau}_1, \frac{1}{\tau}_2, \frac{1}{\tau}_3)$, where τ_i $(i = 1, 2, 3)$ represents the reciprocal of the angle acceleration time constant. T is the sampling interval and equal to the exposure time.

3.2 Measurement prediction

In general, the relationship between measurement and state can be represented by a measurement model, which can be used to predict the measurement. However, the prediction of measurement in this paper is very complex and cannot be represented by a measurement model, but it can be calculated using the following steps.

3.2.1 *Prediction of star trail length*

Because the coordinates of the starting point of the l-th star trail on the image plane are $(u_{l_b}(k), v_{l_b}(k))$, the relationship between physical coordinates $(x'_{l_0}(k), y'_{l_0}(k))$ and $(u_{l_b}(k), v_{l_b}(k))$ can be expressed as

$$\begin{cases} x'_{l_0}(k) = dx\left[u_{l_b}(k) - \dfrac{M}{2}\right], \\ y'_{l_0}(k) = dy\left[v_{l_b}(k) - \dfrac{N}{2}\right], \end{cases} \tag{8}$$

where M and N represent the number of pixels of the image plane in the u and v directions, respectively. The corresponding 3D unit vector of start point can be predicted using

$$\begin{bmatrix} X'_{l_0}(k) \\ Y'_{l_0}(k) \\ Z'_{l_0}(k) \end{bmatrix} = \begin{bmatrix} \dfrac{-x'_{l_0}(k)}{\sqrt{x'_{l_0}(k)^2 + y'_{l_0}(k)^2 + f^2}} \\ \dfrac{-y'_{l_0}(k)}{\sqrt{y'_{l_0}(k)^2 + y'_{l_0}(k)^2 + f^2}} \\ \dfrac{f}{\sqrt{z'_{l_0}(k)^2 + y'_{l_0}(k)^2 + f^2}} \end{bmatrix}, \tag{9}$$

where f is the focus length of the star sensor. The spacecraft is assumed to be moving at uniform speed during the exposure time T, because the exposure time is quite short. The process of estimating the length of a star trail is also divided into 10 segments with respect to the exposure time. The rotation matrix from the starting time instant to the jt time instant can be expressed as

$$\begin{aligned} M_j = &\begin{bmatrix} 1 & 0 & 0 \\ 0 & \cos(w_x(k)\cdot jt) & \sin(w_x(k)\cdot jt) \\ 0 & -\sin(w_x(k)\cdot jt) & \cos(w_x(k)\cdot jt) \end{bmatrix} \\ &\cdot \begin{bmatrix} \cos(w_y(k)\cdot jt) & 0 & -\sin(w_y(k)\cdot jt) \\ 0 & 1 & 0 \\ \sin(w_y(k)\cdot jt) & 0 & \cos(w_y(k)\cdot jt) \end{bmatrix} \\ &\cdot \begin{bmatrix} \cos(w_z(k)\cdot jt) & \sin(w_z(k)\cdot jt) & 0 \\ -\sin(w_x(k)\cdot jt) & \cos(w_x(k)\cdot jt) & 0 \\ 0 & 0 & 1 \end{bmatrix}, \end{aligned} \tag{10}$$

where jt ($j = 1, 2, \ldots, 10; t = \frac{T}{10}$) is the rotation time. The ten 3D unit vectors of the l-th star after the time jt can be expressed as

$$\begin{bmatrix} X'_{l_j}(k) \\ Y'_{l_j}(k) \\ Z'_{l_j}(k) \end{bmatrix} = M_j \begin{bmatrix} X'_{l_0}(k) \\ Y'_{l_0}(k) \\ Z'_{l_0}(k) \end{bmatrix}. \tag{11}$$

The physical coordinates of the l-th star after the time jt can then be calculated by

$$x'_{l_j}(k) = \frac{-X'_{l_j}(k)M}{2\tan(\frac{\mathrm{FOV}_u}{2})Z'_{l_j}(k)}, \quad y'_{l_j}(k) = \frac{-Y'_{l_j}(k)N}{2\tan(\frac{\mathrm{FOV}_v}{2})Z'_{l_j}(k)}, \tag{12}$$

where FOV_u and FOV_v represent the size of the FOV of the star sensor lens in the u and v directions, respectively.

The length of the l-th star trail after interval T can be calculated using the 10 sets of physical coordinates obtained previously:

$$\begin{aligned} d'_l(k) = &\sqrt{(x'_{l_1}(k) - x'_{l_0}(k))^2 + (y'_{l_1}(k) - y'_{l_0}(k))^2} \\ &+ \sqrt{(x'_{l_2}(k) - x'_{l_1}(k))^2 + (y'_{l_2}(k) - y'_{l_1}(k))^2} + \cdots \\ &+ \sqrt{(x'_{l_{10}}(k) - x'_{l_9}(k))^2 + (y'_{l_{10}}(k) - y'_{l_9}(k))^2}. \end{aligned} \tag{13}$$

3.2.2 *Prediction of ending point coordinates*

The coordinates of the ending point $[u'_{l_e}(k), v'_{l_e}(k)]$ of the l-th star trail can be obtained as follows:

$$\begin{cases} u'_{l_e}(k) = \dfrac{x'_{l_{10}}(k)}{dx} + \dfrac{M}{2}, \\ v'_{l_e}(k) = \dfrac{y'_{l_{10}}(k)}{dy} + \dfrac{N}{2}. \end{cases} \tag{14}$$

The predicted measurement is

$$z'_l(k) = \begin{bmatrix} d'_l(k) \\ u'_{l_e}(k) \\ v'_{l_e}(k) \end{bmatrix}, \quad z(k) = \begin{bmatrix} z'_1(k) \\ z'_2(k) \\ \vdots \\ z'_p(k) \end{bmatrix}. \tag{15}$$

3.3 Unscented Kalman filter

As mentioned previously, because the measurement process cannot be described using a measurement model, the extended Kalman filter (EKF) method, which depends on the measurement model, cannot be used. The unscented Kalman Filter (UKF), with its filter schematic shown in Figure 1, is therefore used to estimate the state vector [33].

4 Simulations and analysis

To verify the proposed method under highly dynamical conditions, simulations are implemented as described in this section. A workstation with a 3.20 GHz Intel Core i5 processor and 4G RAM is used for data processing by MATLAB R2015a.

4.1 Simulation conditions

The star sensor frame is coincident with the spacecraft body frame, and the optical axis of the star sensor is assumed to be mounted along the z-axis of the spacecraft. The initial attitude angles in pitch, roll, and yaw are 0°, 90°, and 45°, respectively, for all the simulations. The star sensor used in the experiment is a Cypress STAR1000 CMOS image sensor, which employs a 1024 pixels × 1024 pixels image plane. The element size is 15 μm × 15 μm, as in [27]; this detector has higher responses to wavelengths ranging from 0.55 to 0.85 μm [34]. The focal length is 43.6 mm. The FOV of the star sensor is 20° × 20°. The exposure time is 0.5 s, the star magnitude limit of the star sensor is 5.5 (M_V), and the guide star catalog is selected from Tycho2.

To ensure the realness and effectiveness of the simulated blurred star images, and for the time interval to be quite short, the simulation is divided into 100 frames of star images, which can be considered as a clear star image. The imaging positions of the star points on each clear star image can be determined according to [23]. Given that the imaging process of the star sensor will be interfered with the current, Gaussian white noise with a mean of 0″ and standard deviation of 7″ is added to the imaging position of the star point. Meanwhile, the PSF value of a single star point is set to 5 pixels × 5 pixels ($M_V < 4$) or 3 pixels × 3 pixels ($M_V \geqslant 4$). Finally, the blurred star image can be created through the superposition of the 100 frames of the clear star image.

The window size value of the filter template used in the starting point and ending point determination is set to 5 pixels × 5 pixels. The filtering period of the filter is 0.5 s, and the simulation period is 300 s. The Singer acceleration model parameters are set to $\tau_i = 100$ s. The initial parameters of UKF are as follows.

The initial state vector:

$$\boldsymbol{X}_0 = \left[0\ \text{rad/s}, 0\ \text{rad/s}, 0\ \text{rad/s}, 0\ \text{rad/s}^2, 0\ \text{rad/s}^2, 0\ \text{rad/s}^2\right]^{\mathrm{T}}. \tag{16}$$

The initial matrix of error covariance:

$$\begin{aligned}\boldsymbol{P}_0 =& \text{diag}\big[10^{-5}\ (\text{rad/s})^2, 10^{-5}\ (\text{rad/s})^2, 10^{-5}\ (\text{rad/s})^2,\\ & 10^{-7}\ (\text{rad/s}^2)^2, 10^{-7}\ (\text{rad/s}^2)^2, 10^{-7}\ (\text{rad/s}^2)^2\big].\end{aligned} \tag{17}$$

Case 1: The angular velocity of the spacecraft around all three axes is constant with time:

$$w(t) = [0°/\text{s} \quad 0°/\text{s} \quad 20°/\text{s}]^{\mathrm{T}}. \tag{18}$$

Case 2: The angular velocity of the spacecraft around all three axes changes with time:

$$w_t = \begin{bmatrix} 8\sin(\frac{2\pi}{85}t + \frac{\pi}{2})°/\text{s} \\ 8\sin(\frac{2\pi}{65}t + \frac{\pi}{2})°/\text{s} \\ 8\sin(\frac{2\pi}{45}t + \frac{\pi}{2})°/\text{s} \end{bmatrix}. \tag{19}$$

The angular velocities in cases 1 and 2 are expressed as Figures 2(a) and 3(a), respectively [2, 10], while the angular accelerations corresponding to the angular velocities are illustrated in Figures 2(b) and 3(b), respectively.

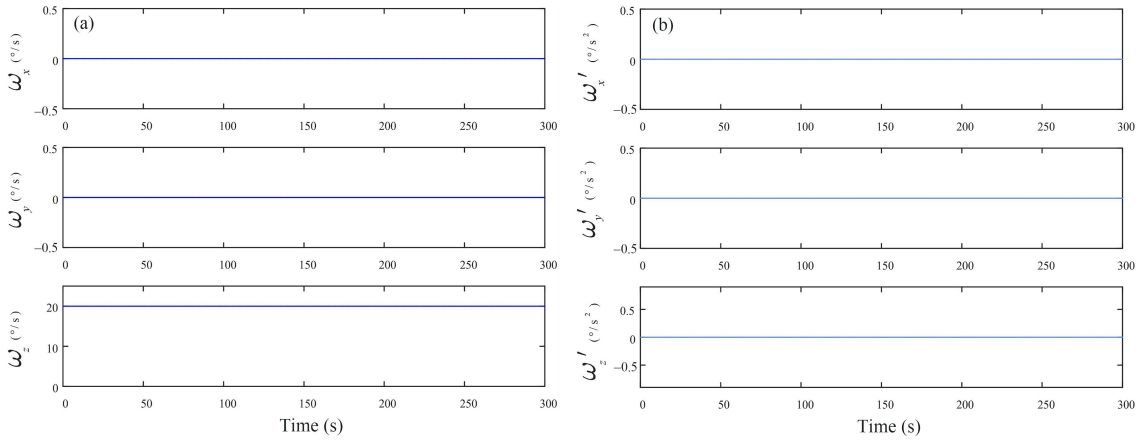

Figure 2 (Color online) Simulated values of (a) three-axis body angular velocity and (b) angular acceleration angular velocity in case 1.

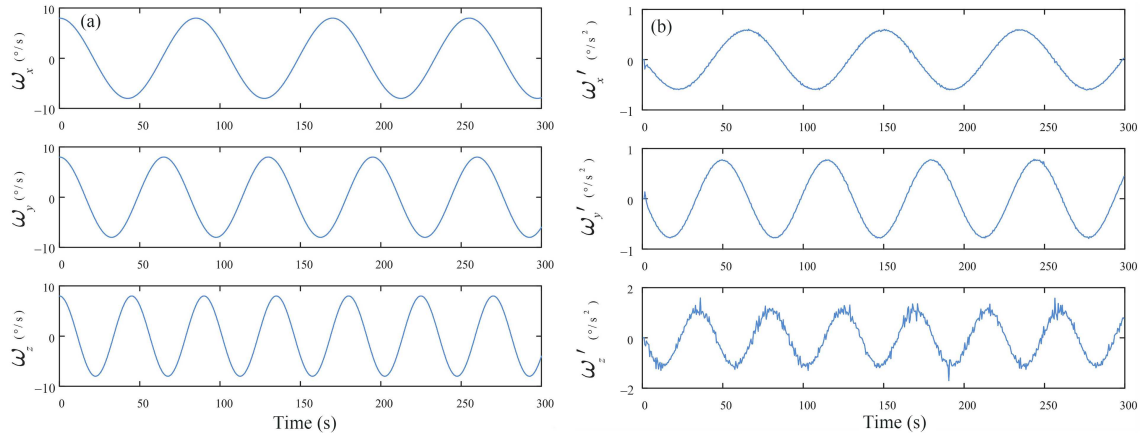

Figure 3 (Color online) Simulated values of (a) three-axis body angular velocity and (b) angular acceleration angular velocity in case 2.

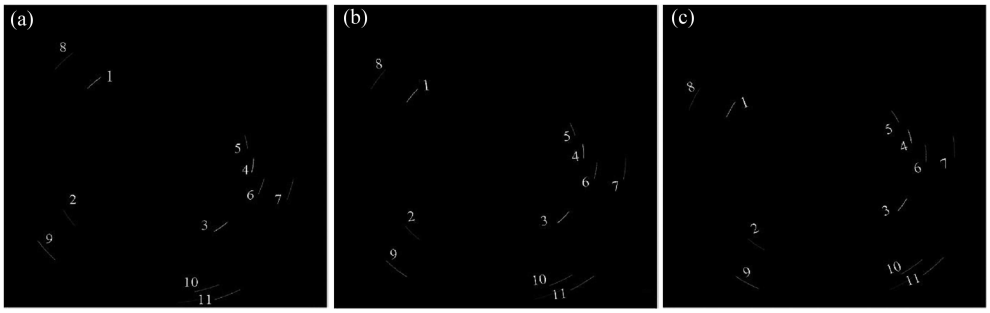

Figure 4 Sequential blurred star images in case 1 with labeled star trails. (a) time = 0.5 s, (b) time = 1.0 s, and (c) time=1.5 s with $w(t) = [0^\circ/\mathrm{s}, 0^\circ/\mathrm{s}, 20^\circ/\mathrm{s}]^{\mathrm{T}}$ and 0.5 s exposure time.

Figures 4 and 5 show three sequential star images from 0.5–1.5 s in cases 1 and 2, respectively. The numbers of useful trails in cases 1 and 2 are visualized in Figure 6. As shown in Figure 4, the star trails are circle arcs revolving around the image center because of the rotation of the spacecraft around the z-axis (optical axis) in case 1, as shown in Figure 6(a), and the number of useful star trails is 11. Figure 5 shows that the sequential blurred images, together with the number of star trails, are changed with respect to time because of the spacecraft in case 2 rotating around three axes, making the stars move out and come into the FOV. Thus, the star numbers change with time, as shown in Figure 6(b).

For example, there are 20 star trails in Figure 5(b): star trails 16 and 17 overlap each other, and star trails 8, 10–13, and 18–23 intersect with the edge of the FOV, and therefore cannot be used in the

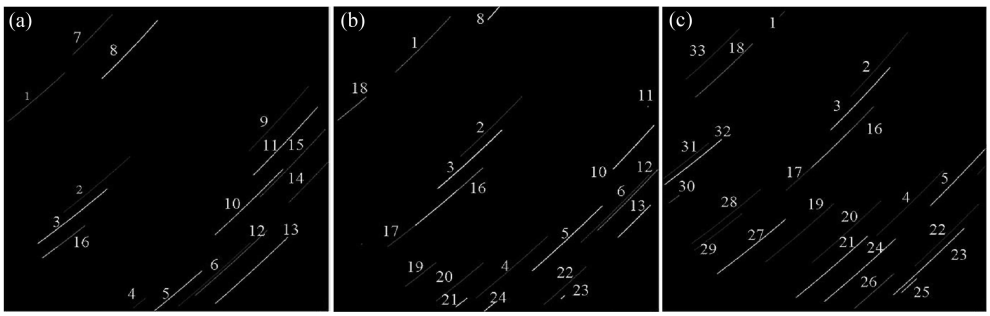

Figure 5 Sequential blurred star images in case 2 with labeled star trails. (a) time = 0.5 s, (b) time = 1.0 s, and (c) time=1.5 s with $w(t) = [8\sin(\frac{2\pi}{85} + \frac{\pi}{2})^\circ/\mathrm{s}, 8\sin(\frac{2\pi}{65} + \frac{\pi}{2})^\circ/\mathrm{s}, 8\sin(\frac{2\pi}{45} + \frac{\pi}{2})^\circ/\mathrm{s}]^{\mathrm{T}}$ and 0.5 s exposure time.

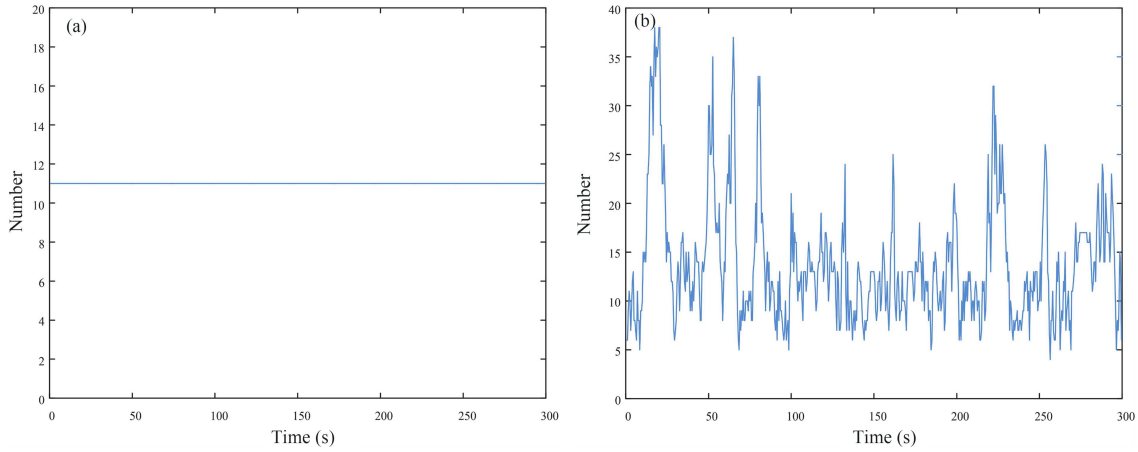

Figure 6 (Color online) Number of available star trails in (a) case 1 and (b) case 2.

estimation process. After selection, the available ones are marked as star trails 1–6.

4.2 Results and analysis

To demonstrate the feasibility and effectiveness of the proposed method, the performance of the proposed method and Accardo's method [25] are compared. Accardo's method uses the velocity vector $\nu = ([u_e, v_e]^{\mathrm{T}} - [u_b, v_b]^{\mathrm{T}})/T$.

4.2.1 *Results for case* 1

For case 1, the angular velocity and angular acceleration estimation results of the two methods are shown in Figures 7 and 8, and Table 1. Figure 7 shows the UKF estimation result of the proposed method: Figures 7(a) and (b) illustrate the estimated values of angular velocity and angular acceleration, respectively, whereas Figures 7(c) and (d) show the statistical charts of the estimation errors of angular velocity and angular acceleration, respectively, relative to the simulation values. Similarly, Figure 8 shows the estimation results of Accardo's method. In Table 1, the mean angular velocity error, mean angular acceleration error, and mean filtering time for one sample time are outlined.

Affected by the poor sensitivity of the star sensor in the direction of the optical axis, a larger estimation error occurs for both methods around the z-axis (optical axis) compared with those around the other axes [2]. As shown in Figure 8, the angular velocity and angular acceleration estimation errors of Accardo's method are periodic, with a period of 18 s, which is consistent with the rotation period of the star trails. This is because Accardo's method uses the velocity vector, which approximates a nonlinear star trail as a linear trail. When u_e and u_b or v_e and v_b of the longest two star trails (Nos. 10 and 11 in Figure 4) are almost equal, large linearized calculation errors of the trail lengths cause large estimation errors around the x and y axes, respectively. The proposed method exhibits a better performance for angular velocity; the angular velocity estimation on the three axes, as shown in Figure 6, are reduced by about 89.8%, 89.8%, and 66.3%, respectively, compared with those of Accardo's method.

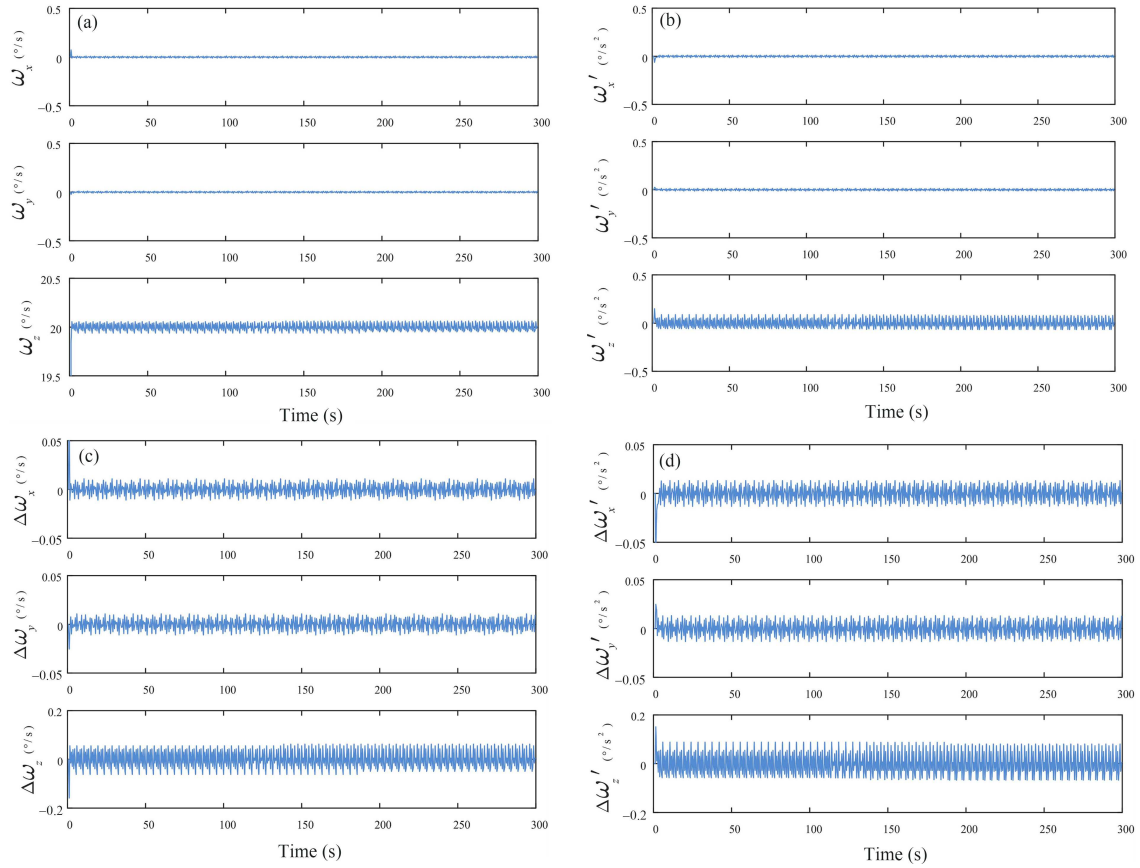

Figure 7 (Color online) Estimation results of proposed method for case 1. (a) Estimated angular velocity; (b) estimated angular acceleration; (c) estimated angular velocity errors; (d) estimated angular acceleration errors.

Table 1 Comparison of angular velocity and angular acceleration errors in case 1

Method	Mean angular velocity error on three axes (°/s)			Mean angular acceleration error on three axes (°/s^2)			Filtering time (one sampling interval) (s)
	x	y	z	x	y	z	
Proposed method	0.005	0.005	0.035	0.007	0.007	0.047	0.025
Accardo's method	0.050	0.050	0.104	0.018	0.018	0.045	0.001

4.2.2 *Results for case 2*

The angular velocity and angular acceleration estimation results for case 2 are shown in Figures 9 and 10, and Table 2. Figure 9 illustrates the UKF estimation results of the proposed method, whereas Figure 10 shows the estimation results of Accardo's method for case 2.

Similar to the results for case 1, the largest estimation error still occurs around the z-axis. Obviously, several peak errors occur around the z-axis, as shown in Figures 9(c) and 10(c). One reason is that some trails in case 2 may also be characterized by u_e and u_b or v_e and v_b that are almost equal, for which large estimation errors are unavoidable, such as the results at $t = 134.5$ s around the x and y axes. Another reason is that the results for case 2 are also affected by the number of star trails. The peak errors occur when the number of star trails is relatively small; for example, peak errors occur at 190.5 and 256.5 s, corresponding to only 5 and 4 stars in Figure 6(b). Meanwhile, the estimated error around the z-axis changes with the period of angular velocity, and large errors occur when angular velocity around the z-axis is 0, as can be seen in Figure 10(c).

However, the proposed method in this study has a more flexible estimation performance, and the angular velocity estimation errors for the three axes are reduced by about 90.8%, 91.6%, and 66.0%, respectively, compared with those of Accardo's method.

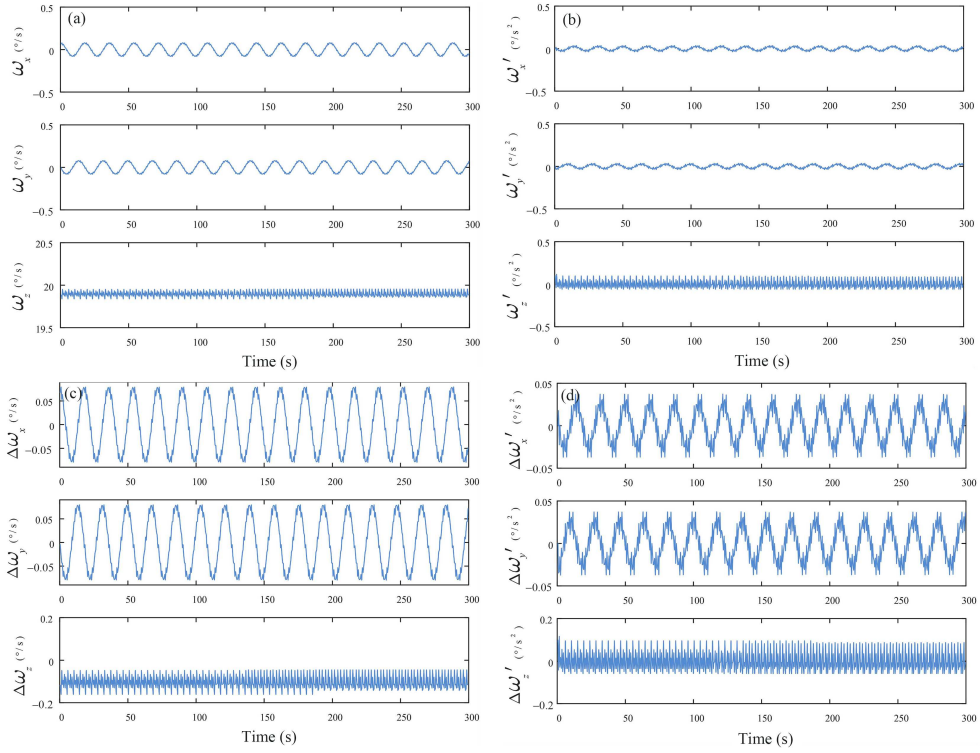

Figure 8 (Color online) Angular velocity estimation results of Accardo's method for case 1. (a) Estimated angular velocity; (b) estimated angular acceleration; (c) estimated angular velocity errors; (d) estimated angular acceleration errors.

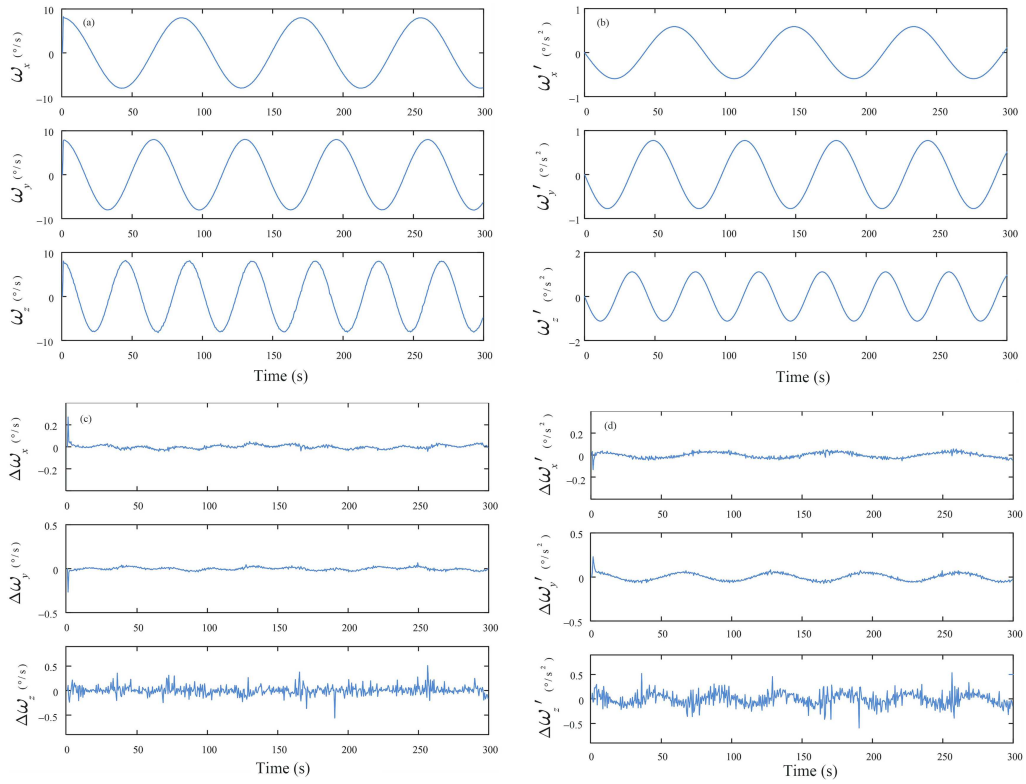

Figure 9 (Color online) Angular velocity estimation results of proposed method for case 2. (a) Estimated angular velocity; (b) estimated angular acceleration; (c) estimated angular velocity errors; (d) estimated angular acceleration errors.

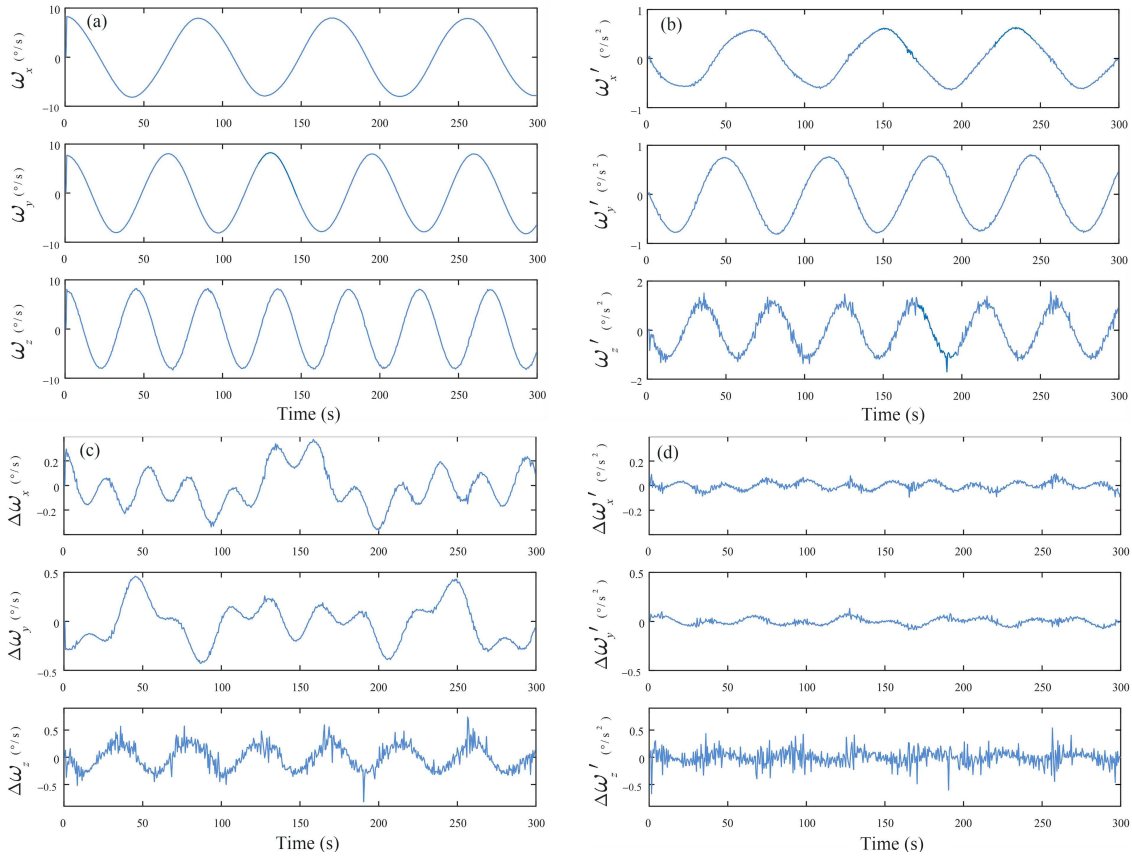

Figure 10 (Color online) Angular velocity estimation results of Accardo's method for case 2. (a) Estimated angular velocity; (b) estimated angular acceleration; (c) estimated angular velocity errors; and (d) estimated angular acceleration errors.

Table 2 Comparison of angular velocity and angular acceleration errors in case 2

Method	Mean angular velocity error on three axes (°/s)			Mean angular acceleration error on three axes (°/s^2)			Filtering time (one sampling interval) (s)
	x	y	z	x	y	z	
Proposed method	0.013	0.013	0.025	0.020	0.034	0.107	0.027
Accardo's method	0.138	0.159	0.001	0.378	0.489	0.729	0.001

5 Conclusion

In this paper, an angular velocity estimation method using the characteristics of star trails for spacecraft is proposed. Trail characteristics directly extracted from blurred star images are used in the process, and the relationship between measurement and state is established. Because the angular velocity estimation method in this paper uses the characteristics of star trails, which is different from Accardo's method, in which the trail is linearized, the method proposed in this paper will not introduce a large linearization error in the case of high angular velocity. Therefore, the estimation error is not sensitive to the angular velocity itself, as can be seen from Figures 7–10, where the angular velocity estimation result of the proposed method is shown to be not sensitive to the angular velocity itself. Simulation results demonstrate that when the angular velocity of the spacecraft is constant, the estimation errors of the proposed method for the three axes are reduced by about 89.8%, 89.8%, and 66.3%, respectively, compared with those of Accardo's method, whereas when the angular velocity of the spacecraft changes with time, the angular velocity estimation errors for the three axes are reduced by about 90.8%, 91.6%, and 66.0%, respectively, compared with those of Accardo's method.

However, like many other methods for estimating angular velocity that are based on star sensors, the angular velocity estimation error around the optical axis of the star sensor is relatively large. In addition,

it is also worth trying more advanced filtering methods [35–38]. We will conduct more in-depth research in the future.

Acknowledgements This work was supported by National Natural Science Foundation of China (Grant No. 61722301). The authors wish to express their gratitude to all members of the Science & Technology on Inertial Laboratory and the Fundamental Science on Novel Inertial Instrument & Navigation System Technology Laboratory for their valuable comments.

References

1 Kudva P, Throckmorton A. Attitude determination studies for the Earth Observation System AM1 (EOS-AM1) mission. J Guid Control Dyn, 1996, 19: 1326–1331
2 Rao G N, Alex T K, Bhat M S. Incremental-angle and angular velocity estimation using a star sensor. J Guid Control Dyn, 2002, 25: 433–441
3 Hajiyev C, Cilden D, Somov Y. Gyro-free attitude and rate estimation for a small satellite using SVD and EKF. Aerospace Sci Tech, 2016, 55: 324–331
4 Shi Z, Yang J, Yue P, et al. Angular velocity estimation in gyroscope-free inertial measurement system based on unscented kalman filter. In: Proceedings of 2010 8th World Congress on Intelligent Control and Automation (WCICA), 2010. 2031–2034
5 Ma H, Xu S. Magnetometer-only attitude and angular velocity filtering estimation for attitude changing spacecraft. Acta Astronaut, 2014, 102: 89–102
6 Pal M, Bhat M. Star sensor based spacecraft angular rate estimation independent of attitude determination. In: Proceedings of 2013 IEEE International Conference on Control Applications (CCA), 2013. 580–585
7 Oshman Y, Markley F L. Sequential attitude and attitude-rate estimation using integrated-rate parameters. J Guid Control Dyn, 1999, 22: 385–394
8 Bar-Itzhack I Y. Classification of algorithms for angular velocity estimation. J Guid Control Dyn, 2001, 24: 214–218
9 Crassidis J L. Angular velocity determination directly from star tracker measurements. J Guid Control Dyn, 2002, 25: 1165–1168
10 Liu H, Yang J, Yi W, et al. Angular velocity estimation from measurement vectors of star tracker. Appl Opt, 2012, 51: 3590–3598
11 Jia H, Yang J K, Li X J, et al. Systematic error analysis and compensation for high accuracy star centroid estimation of star tracker. Sci China Technol Sci, 2010, 53: 3145–3152
12 Schmidt U, Elstner C, Michel K. ASTRO 15 star tracker flight experience and further improvements towards the ASTRO APS star tracker. In: Proceedings of AIAA Guidance, Navigation and Control Conference and Exhibit, 2008. 18–21
13 Xiong K, Jiang J. Reducing systematic centroid errors induced by fiber optic faceplates in intensified high-accuracy star trackers. Sensors, 2015, 15: 12389–12409
14 Jiang J, Wang H, Zhang G. High-accuracy synchronous extraction algorithm of star and celestial body features for optical navigation sensor. IEEE Sens J, 2018, 18: 713–723
15 Silani E, Lovera M. Star identification algorithms: novel approach & comparison study. IEEE Trans Aerosp Electron Syst, 2006, 42: 1275–1288
16 Zhao Y, Wei X, Li J, et al. Star identification algorithm based on K-L transformation and star walk formation. IEEE Sens J, 2016, 16: 5202–5210
17 Markley F L, Crassidis J L. Fundamentals of Spacecraft Attitude Determination and Control. New York: Springer, 2014. 287–343
18 van der Ha J C. Spin-axis attitude determination and covariances in local sun-earth frame. J Guid Control Dyn, 2011, 34: 1720–1727
19 Tang Y, Li J, Wang G. Spacecraft angular velocity estimation algorithm for star tracker based on optical flow techniques. Opt Eng, 2018, 57: 023101
20 Ning X L, Ding Z H, Chen P P, et al. Spacecraft angular velocity estimation method using optical flow of stars. Sci China Inf Sci, 2018, 61: 112203
21 Roshanian J, Yazdani S, Barzamini F. Application of PIV and delaunay triangulation method for satellite angular velocity estimation using star tracker. IEEE Sens J, 2018, 18: 10105–10114
22 Jiang J, Huang J, Zhang G. An accelerated motion blurred star restoration based on single image. IEEE Sens J, 2017, 17: 1306–1315
23 Sun T, Xing F, You Z, et al. Smearing model and restoration of star image under conditions of variable angular velocity and long exposure time. Opt Express, 2014, 22: 6009–6023
24 Zhao J, Zhang C, Yu T, et al. Accuracy enhancement of navigation images using blind restoration method. Acta Astronaut, 2018, 142: 193–200
25 Accardo D, Rufino G. A procedure for three-dimensional angular velocity determination using a star sensor in high-rate rotation modes. Acta Astronaut, 2001, 48: 311–320
26 Fasano G, Rufino G, Accardo D, et al. Satellite angular velocity estimation based on star images and optical flow techniques. Sensors, 2013, 13: 12771–12793

27 Wei X, Zhang G, Fan Q, et al. Star sensor calibration based on integrated modelling with intrinsic and extrinsic parameters. Measurement, 2014, 55: 117–125
28 Otsu N. A threshold selection method from gray-level histograms. IEEE Trans Syst Man Cybern, 1979, 9: 62–66
29 Sun T, Xing F, You Z, et al. Motion-blurred star acquisition method of the star tracker under high dynamic conditions. Opt Express, 2013, 21: 20096
30 Gonzalez R C, Woods R E. Digital Image Processing. Beijing: Publishing House of Electronics Industry, 2017
31 Zhang T Y, Suen C Y. A fast parallel algorithm for thinning digital patterns. Commun ACM, 1984, 27: 236–239
32 Singer R A. Estimating optimal tracking filter performance for manned maneuvering targets. IEEE Trans Aerospace Electr Syst, 1970, 4: 473–483
33 Julier S J, Uhlmann J K. New extension of the Kalman filter to nonlinear systems. In: Proceedings of SPIE, 1997. 3068: 182–193
34 Asadnezhad M, Eslamimajd A, Hajghassem H. Optical system design of star sensor and stray light analysis. J Eur Opt Soc-Rapid Publ, 2018, 14: 1–11
35 Ma L F, Wang Z D, Liu Y R, et al. Distributed filtering for nonlinear time-delay systems over sensor networks subject to multiplicative link noises and switching topology. Int J Robust Nonlin Control, 2019, 29: 2941–2959
36 Ma L, Wang Z, Han Q L, et al. Envelope-constrained H-infinity filtering for nonlinear systems with quantization effects: the finite horizon case. Automatica, 2018, 93: 527–534
37 Ma L F, Wang Z D, Han Q L, et al. Consensus control of stochastic multi-agent systems: a survey. Sci China Inf Sci, 2017, 60: 120201
38 Chen Y G, Wang Z D, Qian W, et al. Finite-horizon H_∞ filtering for switched time-varying stochastic systems with random sensor nonlinearities and packet dropouts. Signal Process, 2017, 138: 138–145